Microwave Imaging of Buried Targets through a Multi-Zooming Approach: Reconstruction Capabilities for Different Object Conductivities

M. Salucci, L. Poli, and A. Massa

Abstract

In this work, the performance of an innovative microwave imaging methodology for buried object detection are analyzed. More precisely, the developed inverse scattering (*IS*) approach is based on a Multi-Frequency (*MF*) formulation of the buried *IS* equations in order to exploit the frequency diversity coming from wideband ground penetrating radar (*GPR*) measurements. The arising *MF* cost function is minimized through a customized deterministic solver based on a conjugate gradient (*CG*) minimizer nested within the iterative multi-scaling approach (*IMSA*) for achieving higher resolutions in the identified regions of interest (*RoI*s). Some illustrative numerical results are shown, in order to verify the effectiveness of the developed *MF-IMSA-CG* methodology when dealing with the retrieval of buried objects having different values of electric conductivity. For completeness, as well as for the sake of comparison, the reconstructions yielded by a competitive state-of-the-art approach based on a frequency hopping (*FH*) processing of the *GPR* spectrum are also shown, by considering several noise conditions.

1 Definitions

1.1 Glossary

- D_{inv}: investigation domain;
- D_{obs}: observation domain;
- N: number of discretization cells in D_{ind};
- V: number of views;
- M: number of measurement points;
- F: number of frequencies considered for the inversion;
- (x_v, y_v): coordinates of the v-th source $(v = 1, \dots, V)$.
- (x_m^v, y_m^v): coordinates of the m-th measurement point for the v-th view v, $(m = 1, \dots, M)$;
- $\varepsilon_{ra} = \frac{\varepsilon_a}{\varepsilon_0}$: relative electric permittivity for the upper half-space $(y > 0)$;
- σ_a: conductivity for the upper half-space $(y > 0)$;
- $\varepsilon_{rb} = \frac{\varepsilon_b}{\varepsilon_0}$: background relative electric permittivity;
- σ_b: background conductivity;

2 Variation of the object conductivity

2.1 Square object ($\varepsilon_{r,obj} = 6.0$)

2.1.1 Parameters

Background

Inhomogeneous and nonmagnetic background composed by two half spaces

- Upper half space ($y > 0$ - air): $\varepsilon_{ra} = 1.0$, $\sigma_a = 0.0$;
- Lower half space ($y < 0$ - soil): $\varepsilon_{rb} = 4.0$, $\sigma_b = 10^{-3}$[S/m];

Investigation domain (D_{inv})

- Side: $L_{D_{inv}} = 0.8$ [m];
- Barycenter: $\left(x_{bar}^{D_{inv}}, y_{bar}^{D_{inv}}\right) = (0.00, -0.4)$ [m];

Time-Domain forward solver ($FDTD$ - $GPRMax2D$)

- Side of the simulated domain: $L = 6$ [m];
- Number of cells: $N^{FDTD} = 750 \times 750 = 5.625 \times 10^5$;
- Side of the $FDTD$ cells $l^{FDTD} = 0.008$ [m];
- Simulation time window: $T^{FDTD} = 20 \times 10^{-9}$ [sec];
- Time step: $\Delta t^{FDTD} = 1.89 \times 10^{-11}$ [sec];
- Number of time samples: $N_t^{FDTD} = 1060$;
- Boundary conditions: perfectly matched layer (PML);
- Source type: Gaussian mono-cycle (first Gaussian pulse derivative, called "Ricker" in $GPRMax2D$)
  - Central frequency: $f_0 = 300$ [MHz];
  - Source amplitude: $A = 1.0$ [A];

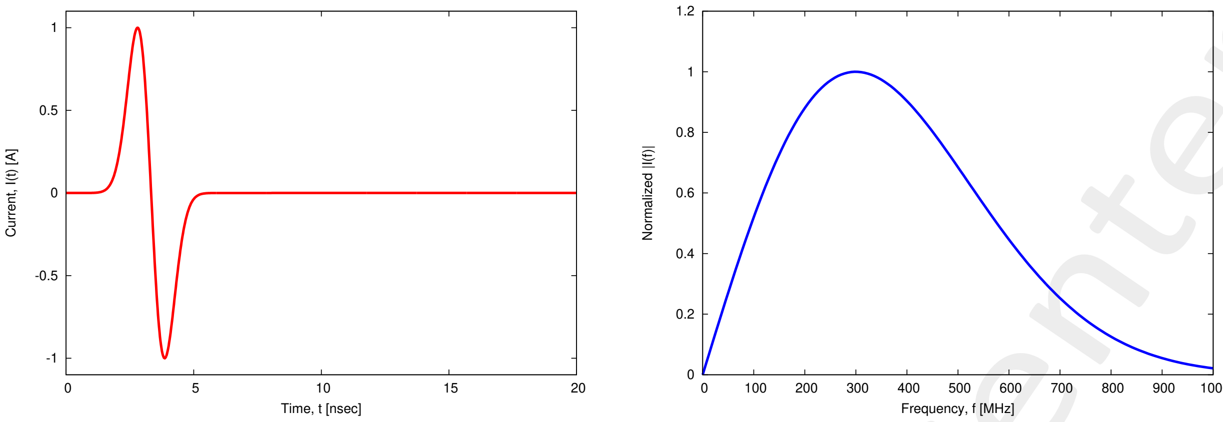

(a) (b)

Figure 1: *GPRMax2D* excitation signal. (a) Time pulse, (b) normalized frequency spectrum.

Frequency parameters

- Frequency range: $f \in [f_{min}, f_{max}] = [200.0, 600.0]$ [MHz] [?] (-3 [dB] bandwidth of the Gaussian Monocycle excitation centered at $f_0 = 300$ [MHz]);
- Frequency step: $\Delta f = 100$ [MHz] ($F = 5$ frequency steps in $[f_{min}, f_{max}]$);

f [MHz]	λ_a [m]	λ_b [m]	f^* [MHz]
200.0	1.50	0.75	200.5
300.0	1.00	0.50	297.6
400.0	0.75	0.37	401.1
500.0	0.60	0.30	498.1
600.0	0.50	0.25	601.6

Table 1: Considered frequencies and corresponding wavelength in the upper medium (λ_a, free space) and in the lower medium (λ_b, soil). f^* is the nearest frequency sample available from transformed time-domain data, and represents the real frequency considered by the inversion algorithm.

Scatterer

- Type: Square;
- Side: 0.16 [m];
- Electromagnetic properties: $\varepsilon_{r,obj} = 6.0$, $\sigma_{obj} = \left\{10^{-4}; 5 \times 10^{-4}; 10^{-3}; 5 \times 10^{-3}; 10^{-2}\right\}$ [S/m];

$\varepsilon_{r,obj}$	σ_{obj} [S/m]	$\Re\{\tau\}$	$\Im\{\tau\}$
6.0	10^{-4}	2.0	2.69×10^{-2}
6.0	5×10^{-4}	2.0	1.49×10^{-2}
6.0	10^{-3}	2.0	0.0
6.0	5×10^{-3}	2.0	-1.19×10^{-1}
6.0	10^{-2}	2.0	-2.69×10^{-1}

Table 2: Real and imaginary parts of the contrast function vs. different values of object conductivity. The imaginary part is computed as $\Im\{\tau\} = \left[\frac{\sigma_b - \sigma_{obj}}{2\pi f \varepsilon_0}\right]$ at the highest frequency ($f_{max} = 600$ [MHz]).

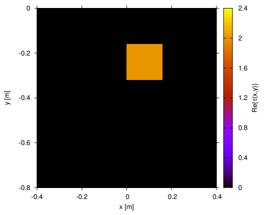

$(a)\ \Re\{\tau\}$

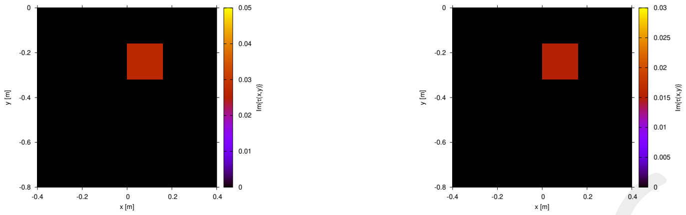

$(b)\ \Im\{\tau\}$ - $\sigma_{obj} = 10^{-4}[\mathrm{S/m}]$ $(c)\ \Im\{\tau\}$ - $\sigma_{obj} = 5 \times 10^{-4}[\mathrm{S/m}]$

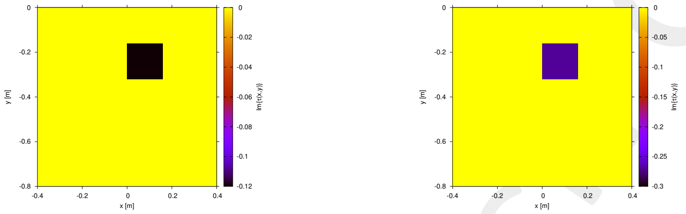

$(d)\ \Im\{\tau\}$ - $\sigma_{obj} = 5 \times 10^{-3}[\mathrm{S/m}]$ $(e)\ \Im\{\tau\}$ - $\sigma_{obj} = 10^{-2}[\mathrm{S/m}]$

Figure 2: Actual object. The imaginary parts are plotted at $f_{max} = 600$ [MHz].

Measurement setup

- Considered frequency: $f_{min} = 200$ [MHz], $\lambda_b = 0.75$ [m].
- $\#DoFs = 2ka = \frac{2\pi}{\lambda_b} L\sqrt{2} = \frac{2\pi}{0.75} 0.8\sqrt{2} \simeq 9.5$;
- Number of views (sources): $V = 10$;
  - $\min\{x_v\} = -0.5$ [m], $\max\{x_v\} = 0.5$ [m];
  - height: $y_v = 0.1$ [m], $\forall v = 1, \dots, V$;
- Number of measurement points: $M = 9$;
  - $\min\{x_m\} = -0.5$ [m], $\max\{x_m\} = 0.5$ [m];
  - height: $y_m = 0.1$ [m], $\forall m = 1, \dots, M$;

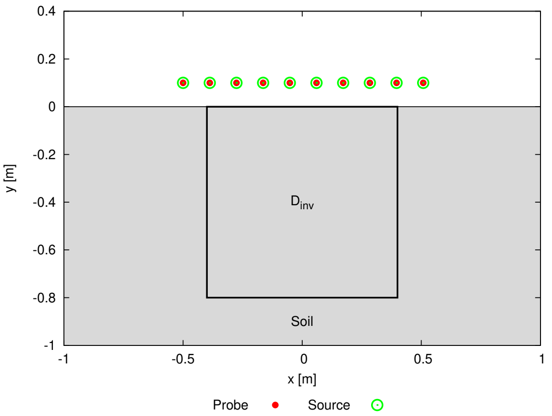

Figure 3: Location of the measurement points ($M = 9$) and of the sources ($V = 10$). Only one source is active for each view.

Inverse solver parameters

- **Shared parameters**
  - Weight of the state term of the functional: 1.0;
  - Weight of the data term of the functional: 1.0;
  - Convergence threshold: 10^{-10};
  - Variable ranges:
    - $\varepsilon_r \in [4.0, 6.2]$;
    - $\Re\left\{E_{tot}^{int}\right\} \in [-8, 8]$, $\Im\left\{E_{tot}^{int}\right\} \in [-8, 8]$;
  - Degrees of freedom:
    - Considered frequency: $f_{min} = 200$ [MHz], $\lambda_b = 0.75$ [m];
    - $\frac{(2ka)^2}{2} = \frac{\left(2\times\frac{2\pi}{\lambda_b}\times\frac{L\sqrt{2}}{2}\right)^2}{2} = 4\pi^2\left(\frac{L}{\lambda_b}\right)^2 = 4\pi^2\left(\frac{0.8}{0.75}\right)^2 \simeq 44.87$;
  - Number of cells: $N = 49 = 7 \times 7$;
  - Maximum number of $IMSA$ steps: $S = 4$;
  - Side ratio threshold: $\eta_{th} = 0.2$;
- $MF - IMSA - CG$ **parameters**
  - Maximum number of iterations: $I = 200$;
- $FH - IMSA - CG$ **parameters**
  - Maximum number of iterations: $I = 400$;

Signal to noise ratio (on $E_{tot}(t)$)

- $SNR = \{50, 40, 30, 20\}$ [dB] + Noiseless data.

2.1.2 $\sigma_{obj} = 10^{-4}$ [S/m] ($\Im\left\{\tau\right\} = 2.69 \times 10^{-2}$): Final reconstructions (@ $f_{max} = 600$ [MHz])

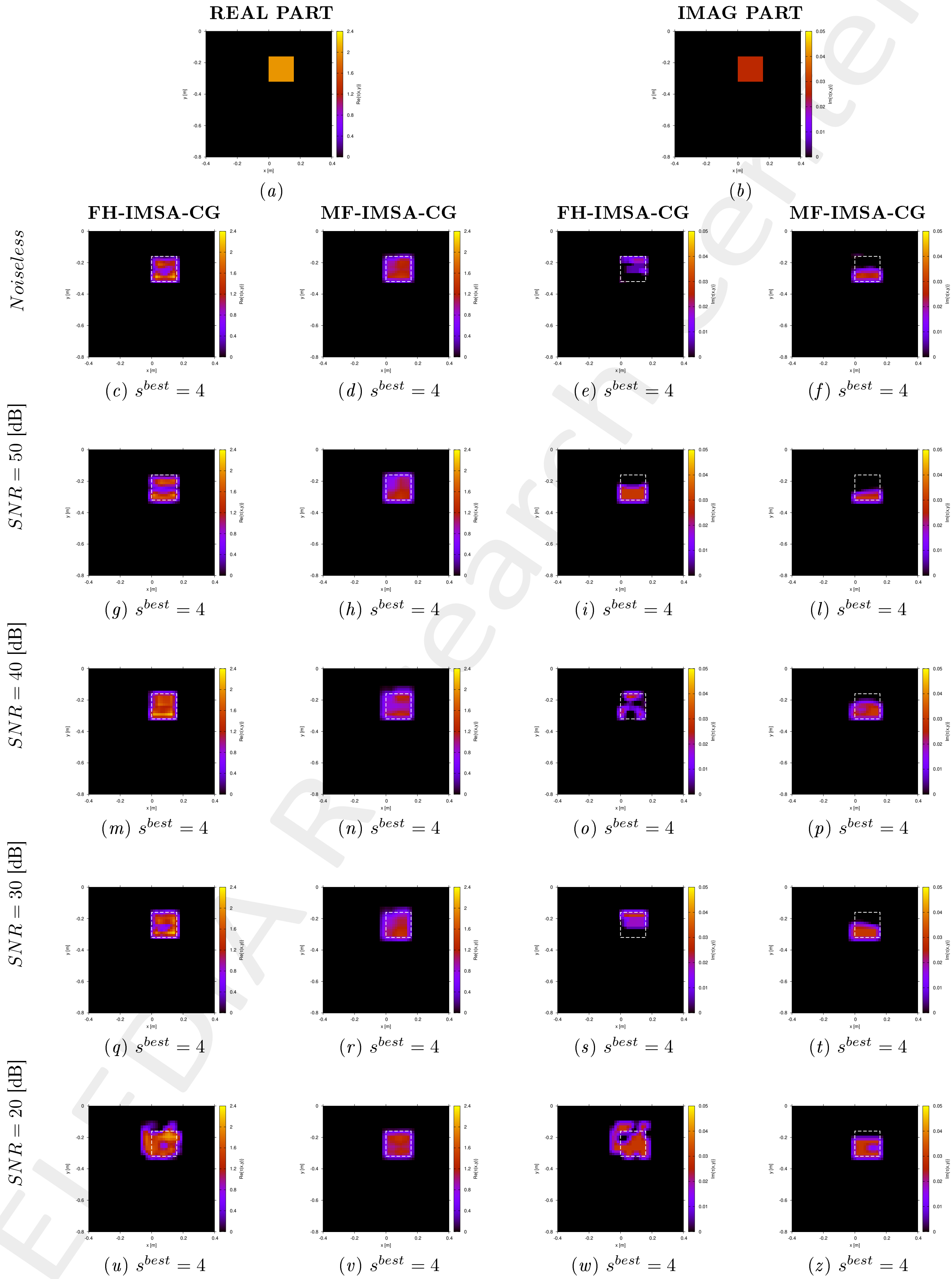

(a) (b)

(c) $s^{best} = 4$ (d) $s^{best} = 4$ (e) $s^{best} = 4$ (f) $s^{best} = 4$

(g) $s^{best} = 4$ (h) $s^{best} = 4$ (i) $s^{best} = 4$ (l) $s^{best} = 4$

(m) $s^{best} = 4$ (n) $s^{best} = 4$ (o) $s^{best} = 4$ (p) $s^{best} = 4$

(q) $s^{best} = 4$ (r) $s^{best} = 4$ (s) $s^{best} = 4$ (t) $s^{best} = 4$

(u) $s^{best} = 4$ (v) $s^{best} = 4$ (w) $s^{best} = 4$ (z) $s^{best} = 4$

Figure 4: $FH-IMSA-CG$ vs. $MF-IMSA-CG$: Retrieved dielectric profiles at the $IMSA$ convergence step (s^{best}).

2.1.3 $\sigma_{obj} = 5 \times 10^{-4}$ [S/m] ($\Im\{\tau\} = 1.49 \times 10^{-2}$): Final reconstructions (@ $f_{max} = 600$ [MHz])

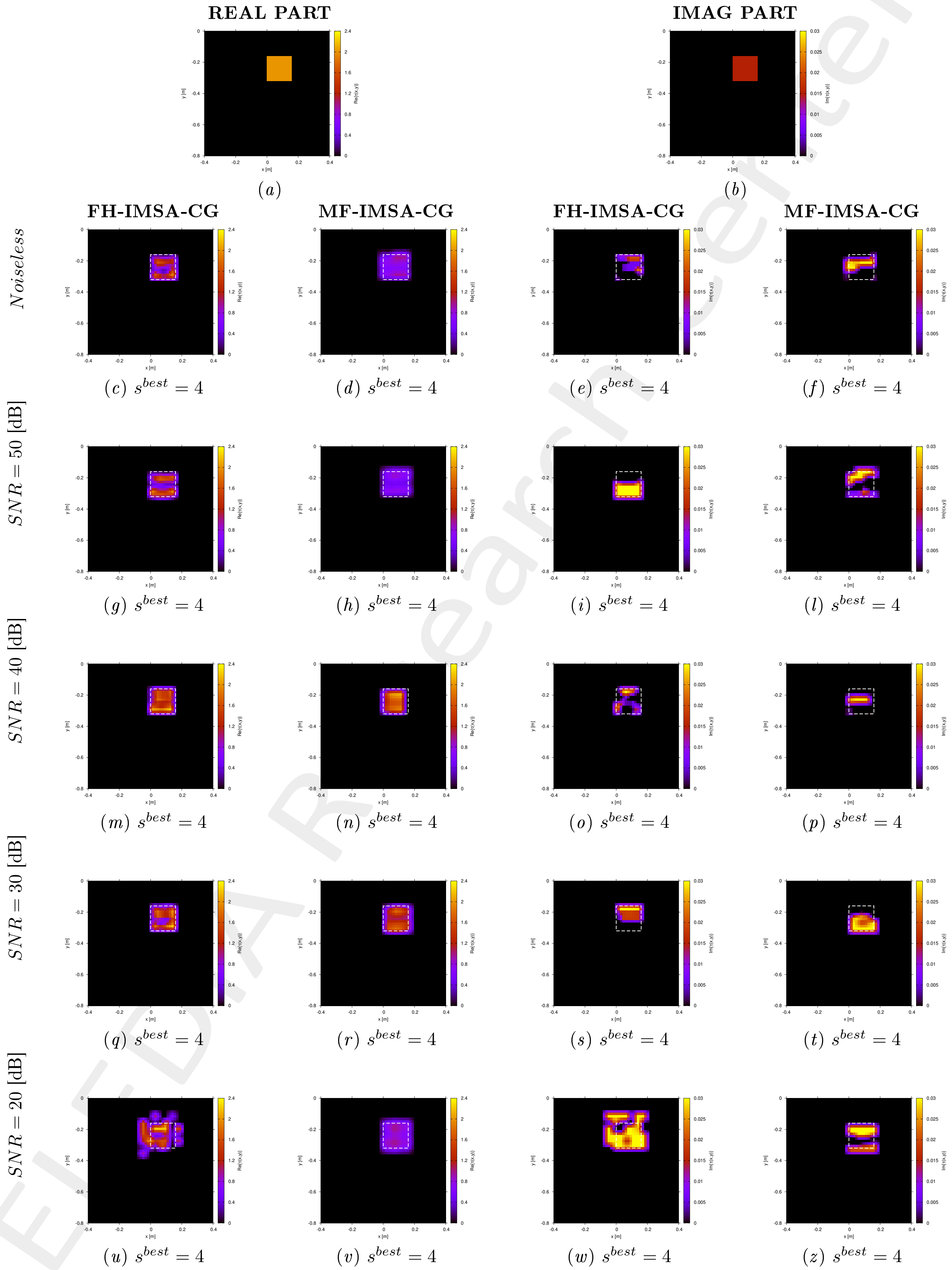

(a) (b)

(c) $s^{best} = 4$ (d) $s^{best} = 4$ (e) $s^{best} = 4$ (f) $s^{best} = 4$

(g) $s^{best} = 4$ (h) $s^{best} = 4$ (i) $s^{best} = 4$ (l) $s^{best} = 4$

(m) $s^{best} = 4$ (n) $s^{best} = 4$ (o) $s^{best} = 4$ (p) $s^{best} = 4$

(q) $s^{best} = 4$ (r) $s^{best} = 4$ (s) $s^{best} = 4$ (t) $s^{best} = 4$

(u) $s^{best} = 4$ (v) $s^{best} = 4$ (w) $s^{best} = 4$ (z) $s^{best} = 4$

Figure 5: $FH-IMSA-CG$ vs. $MF-IMSA-CG$: Retrieved dielectric profiles at the $IMSA$ convergence step (s^{best}).

2.1.4 $\sigma_{obj} = 10^{-3}$ [S/m] ($\Im\{\tau\} = 0.0$): Final reconstructions (@ $f_{max} = 600$ [MHz])

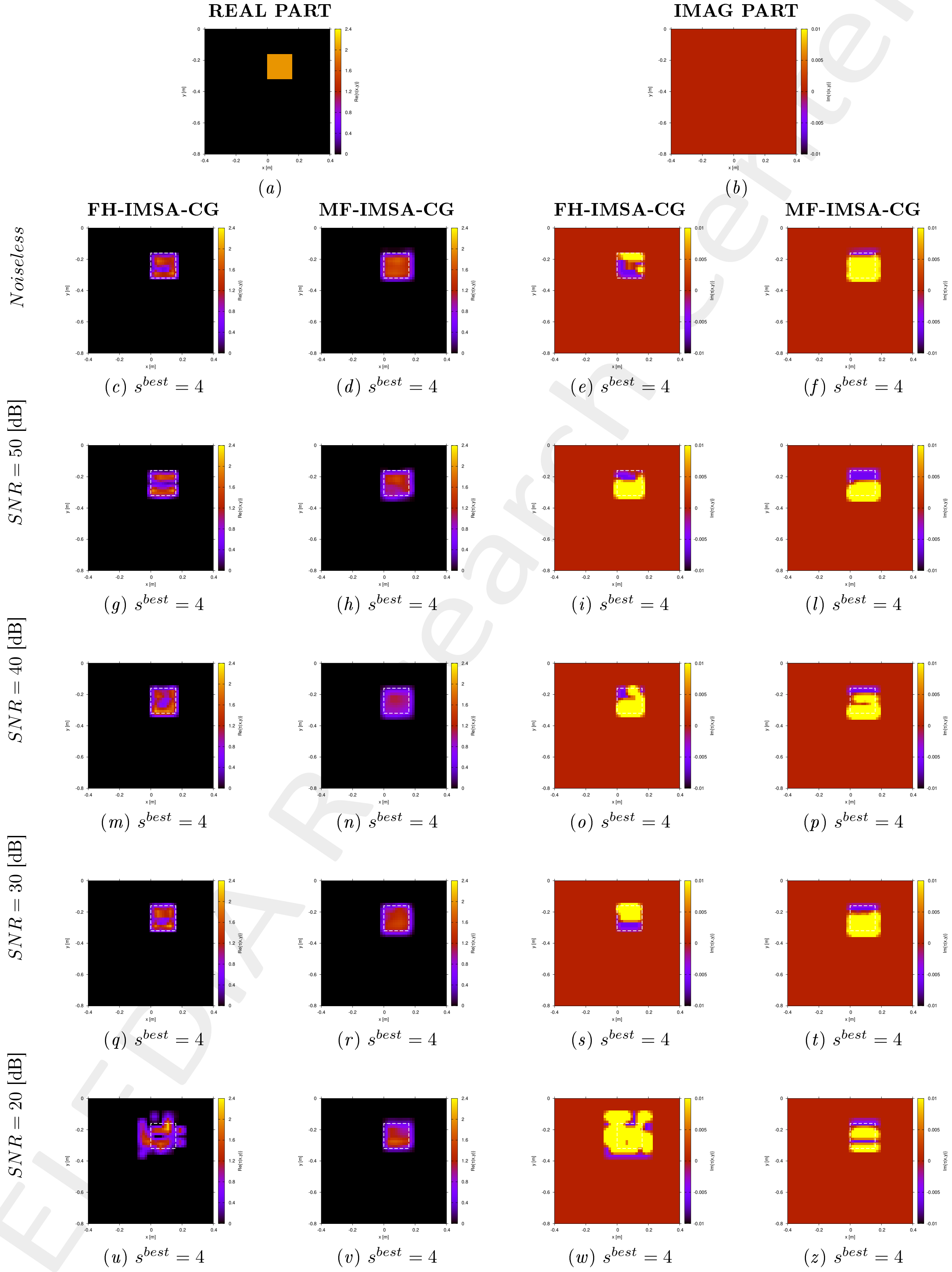

(a) (b)

$(c)\ s^{best} = 4$ $(d)\ s^{best} = 4$ $(e)\ s^{best} = 4$ $(f)\ s^{best} = 4$

$(g)\ s^{best} = 4$ $(h)\ s^{best} = 4$ $(i)\ s^{best} = 4$ $(l)\ s^{best} = 4$

$(m)\ s^{best} = 4$ $(n)\ s^{best} = 4$ $(o)\ s^{best} = 4$ $(p)\ s^{best} = 4$

$(q)\ s^{best} = 4$ $(r)\ s^{best} = 4$ $(s)\ s^{best} = 4$ $(t)\ s^{best} = 4$

$(u)\ s^{best} = 4$ $(v)\ s^{best} = 4$ $(w)\ s^{best} = 4$ $(z)\ s^{best} = 4$

Figure 6: $FH-IMSA-CG$ vs. $MF-IMSA-CG$: Retrieved dielectric profiles at the $IMSA$ convergence step (s^{best}).

2.1.5 $\sigma_{obj} = 5 \times 10^{-3}$ [S/m] ($\Im\{\tau\} = -1.19 \times 10^{-1}$): Final reconstructions (@ $f_{max} = 600$ [MHz])

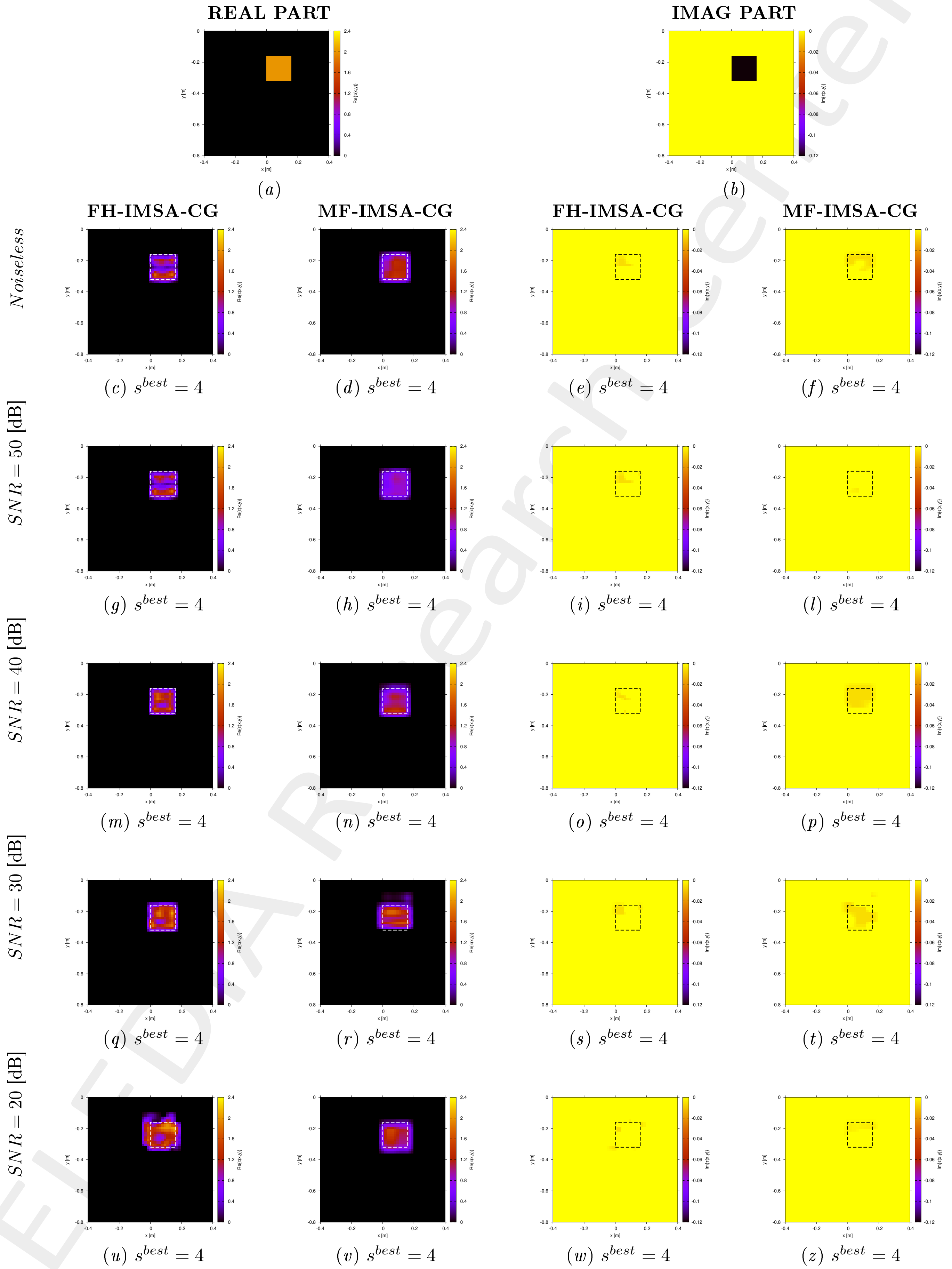

(a) (b)

(c) $s^{best} = 4$ (d) $s^{best} = 4$ (e) $s^{best} = 4$ (f) $s^{best} = 4$

(g) $s^{best} = 4$ (h) $s^{best} = 4$ (i) $s^{best} = 4$ (l) $s^{best} = 4$

(m) $s^{best} = 4$ (n) $s^{best} = 4$ (o) $s^{best} = 4$ (p) $s^{best} = 4$

(q) $s^{best} = 4$ (r) $s^{best} = 4$ (s) $s^{best} = 4$ (t) $s^{best} = 4$

(u) $s^{best} = 4$ (v) $s^{best} = 4$ (w) $s^{best} = 4$ (z) $s^{best} = 4$

Figure 7: $FH-IMSA-CG$ vs. $MF-IMSA-CG$: Retrieved dielectric profiles at the $IMSA$ convergence step (s^{best}).

2.1.6 Errors vs. σ_{obj}

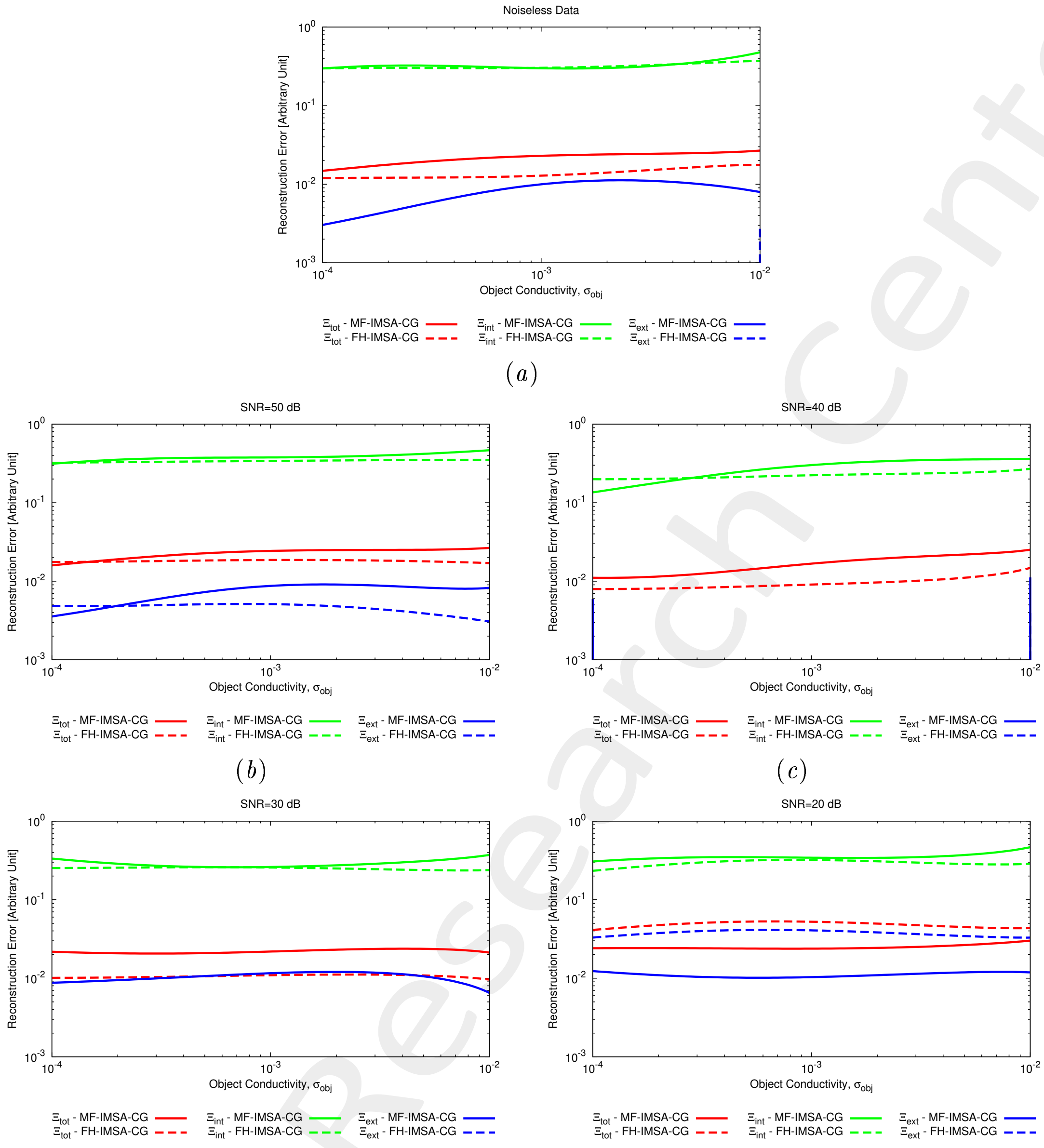

(a)

(b) (c)

(d) (e)

Figure 8: $FH-IMSA-CG$ vs. $MF-IMSA-CG$: Reconstruction errors vs. the object conductivity (σ_{obj}).

More information on the topics of this document can be found in the following list of references.

References

[1] P. Rocca, M. Benedetti, M. Donelli, D. Franceschini, and A. Massa, “Evolutionary optimization as applied to inverse scattering problems,” *Inverse Probl.*, vol. 25, no. 12, pp. 1-41, 2009 (DOI: 10.1088/0266-5611/25/12/123003).

[2] P. Rocca, G. Oliveri, and A. Massa, “Differential Evolution as applied to electromagnetics,” *IEEE Antennas Propag. Mag.*, vol. 53, no. 1, pp. 38-49, Feb. 2011 (DOI: 10.1109/MAP.2011.5773566).

[3] M. Salucci, G. Oliveri, and A. Massa, “GPR prospecting through an inverse scattering frequency-hopping multi-focusing approach,” *IEEE Trans. Geosci. Remote Sens.*, vol. 53, no. 12, pp. 6573-6592, Dec. 2015 (DOI: 10.1109/TGRS.2015.2444391).

[4] M. Salucci, L. Poli, N. Anselmi and A. Massa, “Multifrequency particle swarm optimization for enhanced multiresolution GPR microwave imaging,” *IEEE Trans. Geosci. Remote Sens.*, vol. 55, no. 3, pp. 1305-1317, Mar. 2017 (DOI: 10.1109/TGRS.2016.2622061).

[5] A. Massa, P. Rocca, and G. Oliveri, “Compressive sensing in electromagnetics - A review,” *IEEE Antennas Propag. Mag.*, pp. 224-238, vol. 57, no. 1, Feb. 2015 (DOI: 10.1109/MAP.2015.2397092).

[6] A. Massa and F. Texeira, “Guest-Editorial: Special Cluster on Compressive Sensing as Applied to Electromagnetics,” *IEEE Antennas Wireless Propag. Lett.*, vol. 14, pp. 1022-1026, 2015 (DOI: 10.1109/LAWP.2015.2425011).

[7] N. Anselmi, G. Oliveri, M. Salucci, and A. Massa, “Wavelet-based compressive imaging of sparse targets,” *IEEE Trans. Antennas Propag.*, vol. 63, no. 11, pp. 4889-4900, Nov. 2015 (DOI: 10.1109/TAP.2015.2444423).

[8] G. Oliveri, N. Anselmi, and A. Massa, “Compressive sensing imaging of non-sparse 2D scatterers by a total-variation approach within the Born approximation,” *IEEE Trans. Antennas Propag.*, vol. 62, no. 10, pp. 5157-5170, Oct. 2014 (DOI: 10.1109/TAP.2014.2344673).

[9] T. Moriyama, G. Oliveri, M. Salucci, and T. Takenaka, “A multi-scaling forward-backward time-stepping method for microwave imaging,” *IEICE Electron. Expr.*, vol. 11, no. 16, pp. 1-12, Aug. 2014 (DOI: 10.1587/elex.11.20140578).

[10] T. Moriyama, M. Salucci, M. Tanaka, and T. Takenaka, “Image reconstruction from total electric field data with no information on the incident field,” *J. Electromagnet. Wave.*, vol. 30, no. 9, pp. 1162-1170, 2016 (DOI: 10.1080/09205071.2016.1182876).

[11] F. Viani, L. Poli, G. Oliveri, F. Robol, and A. Massa, “Sparse scatterers imaging through approximated multi-task compressive sensing strategies,” *Microw. Opt. Technol. Lett.*, vol. 55, no. 7, pp. 1553-1557, Jul. 2013 (DOI: 10.1002/mop.27612).

[12] M. Salucci, L. Poli, and A. Massa, “Advanced multi-frequency GPR data processing for non-linear deterministic imaging,” *Signal Processing - Special Issue on ’Advanced Ground-Penetrating Radar Signal-Processing Techniques*,’ vol. 132, pp. 306-318, Mar. 2017 (DOI: 10.1016/j.sigpro.2016.06.019).

[13] M. Salucci, N. Anselmi, G. Oliveri, P. Calmon, R. Miorelli, C. Reboud, and A. Massa, “Real-time NDT-NDE through an innovative adaptive partial least squares SVR inversion approach,” *IEEE Trans. Geosci. Remote Sens.*, vol. 54, no. 11, pp. 6818-6832, Nov. 2016 (DOI: 10.1109/TGRS.2016.2591439).

[14] L. Poli, G. Oliveri, and A. Massa, “Imaging sparse metallic cylinders through a local shape function bayesian compressing sensing approach,” *J. Opt. Soc. Am. A*, vol. 30, no. 6, pp. 1261-1272, Jun. 2013 (DOI: 10.1364/JOSAA.30.001261).